Precise Determination of Deuteron and Neutron Spin Structure Functions at Low to Moderate Q^2 with CLAS

N. Guler,[2,6] R.G. Fersch,[5,7] S.E. Kuhn,[2,*] P. Bosted,[3] K. Griffioen,[5] R. Minehart,[4] and Y. Prok[1,3]

(The CLAS Collaboration)

[1]*Christopher Newport University, Newport News, Virginia 23606*
[2]*Old Dominion University, Norfolk, Virginia 23529*
[3]*Thomas Jefferson National Accelerator Facility, Newport News, Virginia 23606*
[4]*University of Virginia, Charlottesville, Virginia 22901*
[5]*College of William and Mary, Williamsburg, Virginia 23187-8795*
[6]*Present Address: Los Alamos National Laboratory, Los Alamos, New Mexico 87545*
[7]*Present Address: Christopher Newport University, Newport News, Virginia 23606*

(Dated: September 30, 2014)

We present the results for the final analysis of the full data set on spin structure functions of the deuteron collected with Jefferson Lab's CLAS in 2000-2001. Polarized electrons with energies of 1.6, 2.5, 4.2 and 5.8 GeV energy were scattered from deuteron ($^{15}ND_3$) targets dynamically polarized along the beam direction, and detected with CLAS. From the measured double spin asymmetry, polarized structure functions A_1^d and g_1^d were extracted over a wide kinematic range (0.05 GeV$^2 < Q^2 <$ 5 GeV^2 and 0.9 GeV $< W <$ 3 GeV). We use an unfolding procedure to extract from these data and the previously published proton results polarized structure functions A_1^n and g_1^n of the neutron, which are so far unknown in the resonance region. We compare our final results with various theoretical models and expectations as well as parametrizations of the world data. The precision and dense kinematic coverage of these data are unprecedented and will aid in the extraction of polarized parton distributions, tests of pQCD predictions for the quark polarization at large x, a better understanding of quark-hadron duality and more precise values for higher-twist matrix elements in the framework of the Operator Product Expansion.

PACS numbers: 13.60.Hb, 13.88.+e , 14.20.Dh
Keywords: Spin structure functions, nucleon structure

I. INTRODUCTION

One of the enduring goals in the field of hadron physics is a complete picture of how the fundamental particles of the standard model, quarks and gluons, make up the structure and the properties (like total angular momentum and magnetic moment) of the nucleon. Among other observables, inclusive spin structure functions g_1 and g_2 of the nucleon are a vital ingredient for this picture (for a recent review, see [**?**]). For a complete understanding of this parton structure of the nucleon, we need precise and comprehensive data not only for the proton, but also the neutron. Since the two nucleons are isospin partners, one can infer (assuming approximate isospin symmetry) the relative contribution from both up and down valence quarks from measurements on protons and neutrons. Furthermore, there are fundamental sum rules concerning the difference between proton and neutron structure functions at all values of Q^2 that can be tested experimentally. The isoscalar sum of proton and neutron spin structure functions is also most sensitive, via pQCD evolution equations [**?** **?** **?**], to the gluon helicity distribution inside a longitudinally polarized nucleon. Moments of structure functions from proton and neutron access different matrix elements of local operators within the OPE approach [**?** **?** **?**]. Finally, the phenomenon of quark-hadron duality [**?**], observed for proton targets [**?** **?**] needs to be studied for neutrons as well, to rule out that it is just an "accidental" consequence of the particular quark charges in a proton.

Recently, the CLAS collaboration has published [**?**] a comprehensive set of spin structure function data on the proton over a wide range in $Q^2 \approx 0.05 - 5$ GeV^2, and over a wide range of final state masses $W = 0.94 - 3$ GeV. A comparable data set has been collected for the neutron, using polarized ^{3}He as an effective neutron target and the spectrometers in Jefferson Lab's Hall A [**?** **?** **?**]. However, nuclear binding effects have to be corrected for in a model-dependent way to extract neutron structure functions from nuclear data. In particular in the resonance region, where cross sections and asymmetries may vary rapidly with W, Fermi smearing makes the extraction of neutron results challenging and somewhat ambiguous. For that reason, neutron data extracted using an independent method and a different target, namely deuterium, are highly desirable, both to check systematic uncertainties and to more directly access the isoscalar combination $g_1^p + g_1^n$ and its moments. Some deuteron data in the resonance region exist from the RSS experiment [**?**], albeit over a relatively narrow range in Q^2. Many other experiments [**?** **?** **?** **?** **?**] have measured spin structure functions of the deuteron in the deep inelastic (DIS) region $W > 2$ GeV and at large $Q^2 > 1$ GeV^2, or at very small x [**?**]. Very recently, the EG1-DVCS collab-

*Corresponding author.; Electronic address: skuhn@odu.edu

oration has published precise results on the proton and the deuteron at the highest Q^2 accessible with Jefferson Lab so far [**?**].

The present experiment (dubbed "EG1b") collected a comprehensive data set on deuteron ($^{15}ND_3$) targets with nearly equal statistical precision and kinematic coverage as on polarized hydrogen ($^{15}NH_3$). In this paper, we present our final results for the asymmetry $A_1(W,Q^2)$ and the spin structure function $g_1(x,Q^2)$ and its moments for the deuteron. The data have been collected with the CEBAF Large Acceptance Spectrometer (CLAS) in Jefferson Lab's Hall B during the time period 2000 – 2001. Previously, a much smaller data set has been obtained with CLAS in 1998; the results on the deuteron have been published in [**?**]. The present data set was taken with beam energies of 1.6, 2.5, 4.2 and 5.8 GeV. Preliminary results from the highest and lowest beam energies have been published before [**? ? ?**]. The present paper includes, for the first time, the full data set collected with CLAS in 2000-2001 on the deuteron, including experimental and analysis details. We also provide, for the first time, our results for the corresponding neutron structure functions, and the proton-neutron difference, based on a (somewhat model-dependent) "unsmearing" procedure which accounts exactly for Fermi motion in the deuteron [**?**].

Since our analysis of the deuteron data follows closely that for the proton, the present paper is very similar in structure to the previous one [**?**]. In as far as both analyses share the same ingredients and methods, only a brief summary is given here – the reader is referred to [**?**] for details. However, where the two analyses differ, we give all details in what follows. After a brief summary of formalism and theoretical background (Section II), we describe the experimental setup (Section III) and the analysis procedures (Section IV). We present the results for all measured and derived quantities, as well as models and comparison to theory, in Section V, and offer our conclusions in Section VI.

II. THEORETICAL BACKGROUND

A. Formalism

We define the usual kinematic quantities in inclusive lepton scattering: Incident (E) and scattered (E') lepton energy in the lab, scattering angle θ, energy transfer $\nu = E - E'$ and squared four-momentum transfer

$$Q^2 = -q^2 = \vec{q}^2 - \nu^2 = 4EE'\sin^2\frac{\theta}{2}. \quad (1)$$

The 'invariant final state mass is

$$W = \sqrt{(p+q)^2} = \sqrt{M^2 + 2M\nu - Q^2}, \quad (2)$$

and the Bjorken scaling variable,

$$x = \frac{Q^2}{2M\nu}, \quad (3)$$

(M is the nucleon mass). The following variables are also used:

$$\gamma = \frac{2Mx}{\sqrt{Q^2}} = \frac{\sqrt{Q^2}}{\nu}, \tau = \frac{\nu^2}{Q^2} = \frac{1}{\gamma^2}, \quad (4)$$

and the virtual photon polarization ratio

$$\epsilon = \left(1 + 2[1+\tau]\tan^2\frac{\theta}{2}\right)^{-1}. \quad (5)$$

B. Cross sections and asymmetries

The observable measured in EG1b is the double spin asymmetry

$$A_{||}(\nu, Q^2, E) = \frac{d\sigma^{\uparrow\Downarrow} - d\sigma^{\uparrow\Uparrow}}{d\sigma^{\uparrow\Downarrow} + d\sigma^{\uparrow\Uparrow}} \quad (6)$$

for inclusive electron deuteron scattering with beam and target spin parallel ($\uparrow\Uparrow$) or antiparallel ($\uparrow\Downarrow$) along the beam direction. It depends on the four structure functions [1] F_1^d, F_2^d, g_1^d and g_2^d. Introducing the ratio R of longitudinal to transverse virtual photon absorption cross section,

$$R = \frac{\sigma_L(\gamma^*)}{\sigma_T(\gamma^*)} = \frac{F_2}{2xF_1}(1+\gamma^2) - 1 \quad (7)$$

and

$$D = \frac{1 - E'\epsilon/E}{1+\epsilon R}, \eta = \frac{\epsilon\sqrt{Q^2}}{E - E'\epsilon} \quad (8)$$

we can express $A_{||}$ as:

$$\frac{A_{||}}{D} = (1+\eta\gamma)\frac{g_1}{F_1} + [\gamma(\eta-\gamma)]\frac{g_2}{F_1}. \quad (9)$$

Alternatively, the double spin asymmetry $A_{||}$ can also be interpreted in terms of the two virtual photon asymmetries A_1 and A_2:

$$A_{||} = D[A_1(\nu,Q^2) + \eta A_2(\nu,Q^2)]. \quad (10)$$

These quantities can be related back to the structure functions. In particular, given a model or other information for F_1, R and A_2, A_1 can be extracted directly from Eq. 10 and g_1 from

$$g_1 = \frac{\tau}{1+\tau}\left(\frac{A_{||}}{D} + (\gamma - \eta)A_2\right)F_1. \quad (11)$$

(Our deuteron data are not sensitive enough to A_2 or g_2 to extract these quantities; instead a model based on other existing data is used - see below.)

[1] In principle, the tensor structure function b_1 also enters in the denominator, since any realistic polarized target will have a non-zero tensor polarization P_{zz}. However, this is a small correction which is properly taken into account in our extraction of physics results.

C. Virtual photon absorption asymmetry

The asymmetry A_1 can be interpreted both in terms of transition amplitudes for resonant excitations (at $W < 2$, *i.e.* in the resonance region) as well as in terms of the underlying quark helicity distributions (in the DIS region). In the former case, the measured asymmetry A_1 at a given value of W gives information on the helicity structure of both resonant and non-resonant contributions to the inclusive cross section, and can help to constrain the spin-isospin structure of nucleon resonances.

In the DIS region, $A_1(x)$ can yield information on the polarization of the valence quarks at sufficiently large x. In the naive parton model, and without taking nuclear effects into account, the limit of $A_{1d}(x)$ at large x is given as

$$A_{1d} \approx \frac{\Delta u_v + \Delta d_v}{u_v + d_v} = \frac{\Delta u_v/u_v + (d_v/u_v)\Delta d_v/d_v}{1 + d_v/u_v} \quad (12)$$

where u_v, d_v are the unpolarized up- and down valence quark distributions and $\Delta u_v, \Delta d_v$ the corresponding helicity distributions. In a naive $SU(6)$-symmetric, nonrelativistic quark model, $\Delta u/u = 2/3$ and $\Delta d/d = -1/3$, while $d/u = 1/2$, yielding $A_{1d} = 1/3$. On the other hand, most realistic models predict that $A_{1d}(x) \to 1$ as $x \to 1$ due to SU(6) symmetry breaking, albeit with significant differences between the models. In particular, relativistic constituent quark models [**?**] predict a much slower rise towards $A_1 = 1$ than perturbative QCD calculations [**?** **?**] incorporating helicity conservation. Recently, modifications of the pQCD picture including orbital angular momentum [**?**] have yielded an intermediate approach towards $x = 1$. Precise measurements of A_1 at large x and in the DIS region are therefore required for both protons and neutrons or deuterons to establish the validity of these predictions.

D. The spin structure function g_1

The structure function $g_1(x, Q^2)$ contains most of the available information on the internal spin structure of the nucleon. In the DIS limit (large Q^2 and ν), it encodes the polarized parton densities (PDFs) $\Delta q(x) = q\uparrow(x) - q\downarrow(x)$ for quarks with helicity aligned *vs.* antialigned with the overall (longitudinal) nucleon spin. Its logarithmic Q^2 dependence contains, via the QCD evolution equations [**?** **?** **?**], information on the helicity- dependent gluon PDFs $\Delta G(x)$ as well. The deuteron, as an approximate isoscalar nucleon target, is particularly sensitive to $\Delta G(x)$, given a sufficiently large range in Q^2. Jefferson Lab data like the ones presented in this paper can serve as valuable anchor point at the lowest possible Q^2 for such extractions.

In the region of lower Q^2, additional scaling violations occur due to higher-twist contributions, leading to correction terms proportional to powers of $1/Q^2$. These corrections can be extracted from our data since they cover seamlessly the transition from $Q^2 \ll 1$ GeV^2 to the scaling region $Q^2 > 1$ GeV^2. In the kinematic region where ν is also small and therefore $W < 2$ GeV, the structure of g_1 is dominated by the contributions from nucleon resonances (similarly to A_1).

However, as already observed by Bloom and Gilman [**?**] for the unpolarized proton structure function F_2, there seems to be some duality between structure functions in the resonance region (averaged over a suitable range in W) and their extrapolated DIS values at the same quark momentum fraction x or $\xi = \frac{|\vec{q}|-\nu}{M}$. This correspondence should be tested for both nucleon species and for polarized as well as unpolarized structure functions to elucidate the underlying dynamics. EG1 data have uniquely suitable kinematic coverage stretching from the resonance to the DIS region to test whether duality holds for g_1.

E. Quasi-elastic scattering

The virtual photon asymmetries A_1 and A_2 are also defined for elastic scattering off the nucleon and the same relationship Eq. 10 applies. One can show that $A_1 = 1$ in this case, and

$$A_2(Q^2) = \sqrt{R} = \frac{G_E(Q^2)}{\sqrt{\tau} G_M(Q^2)}, \quad (13)$$

where G_E and G_M are the electric and magnetic Sachs form factors of the nucleon.

One can also extend the definition of $g_1(x)$ and $g_2(x)$ for the nucleon to include elastic scattering, $x \equiv 1$:

$$\begin{aligned} g_1^{el}(x, Q^2) &= \frac{1}{2} \frac{G_E G_M + \tau G_M^2}{1+\tau} \delta(x-1) \\ g_2^{el}(x, Q^2) &= \frac{\tau}{2} \frac{G_E G_M - G_M^2}{1+\tau} \delta(x-1). \end{aligned} \quad (14)$$

For a bound system like deuterium, one has to consider the initial state (Fermi-) motion of the struck nucleons. In quasi-elastic inclusive scattering, $W \lesssim 1$ GeV, both the neutron and the proton contribute (weighed by their elastic cross sections). Alternatively, if one detects the struck proton in addition to the scattered electron (with small missing four-momentum), the asymmetry $A_{||}$ will be very close to that on a free proton. In both cases, the theoretical asymmetry can be calculated with reasonable precision (given a realistic deuteron wave function) and therefore the measured asymmetry can be used to extract the product of target and beam polarization (see below).

F. Moments

In addition to the structure function $g_1(x)$ itself, its moments (integrals over x weighted by powers of x) are of great interest. Within the Operator Product Expansion formalism, these moments can be related to local operators [**?**]. They are constrained by several sum rules and can be calculated directly within lattice QCD or in effective field

theories like Chiral Perturbation Theory (χPT) [**?** **?**]. Determining these moments over a range of Q^2 allows us to study the transition from hadronic (resonance) degrees of freedom to partonic ones in our description of the nucleon, and to extract higher twist matrix elements that are sensitive to quark-gluon correlations in the nucleon.

The first moment of g_1,

$$\Gamma_1(Q^2) \equiv \int_0^1 g_1(x,Q^2)dx, \tag{15}$$

can be related to the contributions Δq of the quark helicities to the nucleon spin in the limit of very high Q^2. In particular, for the average of proton and neutron (the "isoscalar nucleon" approximated by the deuteron) one has

$$\frac{\Gamma_1^{p+n}(Q^2\to\infty)}{2} \approx \Gamma_1^d = \frac{5}{36}(\Delta u + \Delta d) + \frac{1}{18}\Delta s. \tag{16}$$

Forming the difference between proton and the neutron yields the famous Bjorken sum rule [**?** **?**]:

$$\Gamma_1^p - \Gamma_1^n = \frac{1}{6}a_3 = 0.211 \tag{17}$$

where $a_3 = g_A = 1.267 \pm 0.004$ is the neutron axial beta decay constant.

At high but finite Q^2, these moments receive pQCD corrections, which allows us to extract information on the polarized gluon distribution $\Delta G(x)$. At the even lower Q^2 of the present data, additional corrections due to higher twist matrix elements and proportional to powers of $1/Q^2$ become important:

$$\Gamma_1(Q^2) = \mu_2(Q^2) + \frac{M^2}{9Q^2}\left(a_2(Q^2) + 4d_2(Q^2) + 4f_2(Q^2)\right) + \cdots \tag{18}$$

Here, μ_2 is the leading twist contribution given by Eq. 16 plus pQCD corrections, a_2 and d_2 are due to target mass corrections and f_2 is a twist-4 matrix element that contains information on quark-gluon correlations and has been calculated using quark models [**?**], QCD sum rules [**?**] and other approaches [**?**].

In addition to the leading first moment, odd-numbered higher moments of g_1 can be defined as $\Gamma_1^n = \int_0^1 dx x^{n-1} g_1(x)$, $n = 3, 5, 7, ...$ These moments are dominated by high x (valence quarks) and are thus particularly well determined by Jefferson Lab data. They can also be related to hadronic matrix elements of local operators or (in principle) evaluated with Lattice QCD methods. The third moment Γ_1^3 is related to the matrix element a_2 above.

In the limit of very small photon virtualities Q^2, moments of spin structure functions can be connected to observables in Compton scattering. In particular, the first moment is constrained by the Gerasimov-Drell-Hearn (GDH) sum rule [**?** **?**] in the limit $Q^2 \to 0$:

$$\left.\frac{d\Gamma_1(Q^2)}{dQ^2}\right|_{Q^2=0} = -\frac{\kappa^2}{8M^2}, \tag{19}$$

where κ is the anomalous magnetic moment of the nucleon. Higher order derivatives at the photon point are, in principle, calculable via χPT [**?** **?**]. Therefore, measuring Γ_1 over the whole range in Q^2 yields a stringent test of our understanding of strongly interacting matter at all length scales.

Extending the analysis of low-energy Compton amplitudes to higher orders, one can get additional generalized sum rules [**?**]. In particular, one can generalize the forward spin polarizability, γ_0, to virtual photons:

$$\gamma_0(Q^2) = \frac{16\alpha M^2}{Q^6}\int_0^1 x^2\left[g_1(x,Q^2) - \gamma^2 g_2(x,Q^2)\right]dx. \tag{20}$$

Once again, this generalized spin polarizability can be calculated (in principle) using χPT [**?**].

G. From nucleons to the deuteron

Most of the previous discussion is focused on the interpretation of spin structure functions of the nucleon (proton and neutron). Where appropriate, we indicate how this interpretation may be modified when the nucleons are embedded in deuterium. Here, we want to discuss in more detail how the nuclear structure of the deuteron affects the measured asymmetries and structure functions.

In the most simple-minded picture, all observables on the deuteron can be considered (cross section weighted) averages of the corresponding proton and neutron observables. Spin observables are further modified by the fact that even in a fully polarized deuteron, the nucleon spins are not 100% aligned due to the D-state component of the wave function. At first order, this can be corrected for by applying a reduction by a factor $(1 - 1.5P_D)$ to all nucleon spin observables inside deuterium, with $P_D \approx 5\%$ being the D-state probability (according to recent models of the deuteron wave function [**?**]). Taking this factor into account, the spin structure functions $g_1^D(x)$ and $g_2^D(x)$ of the deuteron are reasonably well approximated by the average of the proton and neutron ones, as long as x is not too large ($x < 0.6$) and one is not in the resonance region ($W > 2$ GeV). Moments of these structure functions are also relatively "safe" since the integration averages over effects like Fermi motion.

In the valence region of moderate to large x and in the resonance region, Fermi-smearing due to the intrinsic motion of the nucleons inside deuterium as well as nuclear binding become more important, because structure functions vary rapidly in this region with W or x. These binding effects can be modeled by convoluting the free nucleon structure functions with the momentum distribution of nucleons inside deuterium. In our analysis, we use a recent convolution model by Melnitchouk et al. [**?**] that properly treats the effects of finite momentum transfer Q^2.

Beyond the effects discussed so far, one has to consider potential off-shell effects (due to the negative binding energy of nucleons inside deuterium), including perhaps a modification of the nucleon structure ("EMC effect"). Fi-

nally, non-nucleonic degrees of freedom (mesons, $\Delta\Delta$ components and perhaps more exotic quark structures) as well as final state interactions may play a role. Since no universally accepted model for these effects exists, we don't correct for them but include an estimate of their magnitude in our systematic error on the extracted neutron observables. Given the small binding energy (-2.2 MeV) and large average inter-nucleon distance (of order 4 fm) in deuterium, we expect such effects to be significantly smaller than in more tightly bound nuclei. However, a comparison with neutron spin observables obtained from measurements on ^{3}He can be a valuable cross check of these assumptions. Ultimately, the best approach to extracting free neutron information would be to apply the method of spectator tagging (pioneered for unpolarized structure functions in the recent "BONuS" experiment [**?**] at Jefferson Lab).

III. THE EXPERIMENT

The EG1b experiment took place at Jefferson Lab over 7 months in 2000-2001. It used the highly polarized (up to 85%) electron beam produced by the continuous wave electron beam accelerator ("CEBAF"), with energies from 1.6 GeV to nearly 6 GeV and currents of 0.3 nA to 10 nA in the experimental Hall B. Detailed descriptions of the accelerator and its strained GaAs polarized electron source can be found in Refs. [**? ? ? ?**].

The beam polarization was intermittently monitored using a Møller polarimeter, and the beam position and intensity distribution was measured with a set of beam monitors. The amount of beam charge delivered to the Hall for a given time interval was measured with a Faraday cup (FC). The signal from this FC was recorded separately for each "bucket" of a given beam polarization and gated by the data acquisition life time. In order to avoid local heating and depolarization, the beam was rastered over the face of the target in a spiral pattern, using 2 magnets upstream of the target.

The target consisted of cells containing samples of polarized hydrogen ($^{15}NH_3$), deuterium ($^{15}ND_3$), carbon, or no solid material ("empty target") that could be alternatively inserted in the beam. These cells where suspended in a liquid ^{4}He bath at about 1 K. The target material was polarized inside a 5 T solenoidal field along the beam axis, using the method of dynamic nuclear polarization (DNP) described in [**? ? ?**]. The target polarization was monitored by an NMR system. Typical values of about 30% deuteron polarization along or opposite to the beam direction where achieved during the experiment.

Scattered electrons (and other particles) were detected with the CEBAF Large Acceptance Spectrometer (CLAS) [**?**] in Hall B. CLAS employs a toroidal magnetic field and several layers of detectors in 6 identical sectors surrounding the beam axis for an acceptance of nearly 2π in azimuth. Electrons could be detected in the scattering angle range from 8° to about 50°. Three regions of drift chambers (DC) [**?**] determine charged particle tracks, followed by Cherenkov counters (CC) [**?**] and electromagnetic calorimeters (EC) [**?**] for electron identification, while timing is provided by an extensive scintillation counter (SC) system [**?**].

The experimental setup and operation is described in detail in the companion paper on our proton results [**?**].

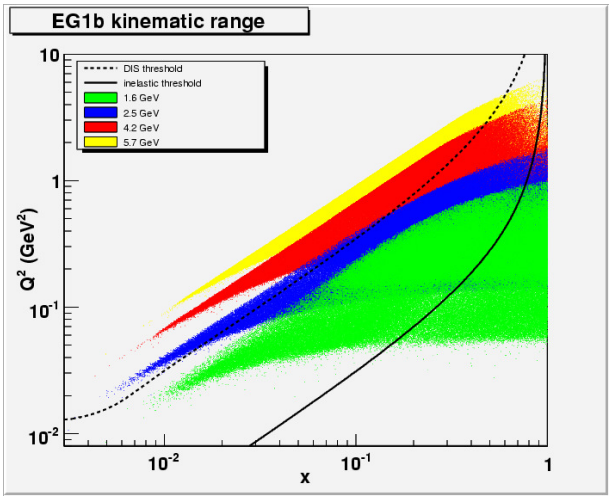

FIG. 1: Kinematic coverage in Q^2 vs. x for each of the 4 main electron beam energy "groupings" used in the EG1b experiment. The solid and dotted lines denote the W =1.07 and 2.00 GeV thresholds, respectively. The coverage for proton (NH_3) and deuterium (ND_3) targets was nearly identical.

IV. DATA ANALYSIS

A. Data set

Data on the deuteron (ND_3) were taken with 7 different beam energies and two configurations of the CLAS torus magnetic field. In the so-called inbending ("+") configuration, the magnetic field would bend electrons inwards, which reduced the acceptance at small angles (small Q^2) but allowed us to run with the highest possible luminosity. In the outbending ("–") configuration, electrons where detected down to angles of 8°, extending the data set to lower Q^2 but requiring us to run with lower beam currents (to avoid overloading the data acquisition) and therefore reducing the statistics collected at higher Q^2.

In all, data were collected in 11 specific combinations ($1.606+$, $1.606-$, $1.723-$, $2.561+$, $2.561-$, $4.238+$, $4.238-$, $5.615+$, $5.725+$, $5.725-$, $5.743-$) of beam energy (in GeV) and main torus polarity ($+$,$-$), hereby referred to as "sets". Sets with similar beam energy comprise four "groupings" with nominal average energies of 1.6, 2.5, 4.2 and 5.8 GeV. The kinematic coverage of the data for each of the 4 energy groupings is demonstrated in Fig. 1.

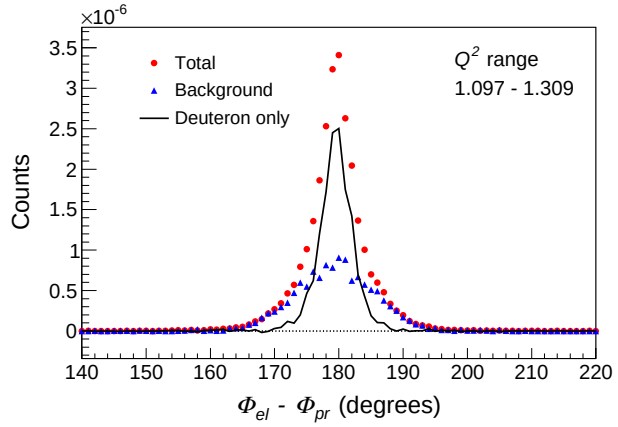

FIG. 2: Distribution of quasielastic $d(e,e'p)$ events over the angle ϕ between the azimuth of the scattered electron and the azimuth of the observed proton The background due to nitrogen, liquid ^{4}He and various foils is strongly suppressed by the cuts described in the text, leading to a clean signal from the deuteron component of the target. A final cut is applied from $\phi = 177^\circ$ to 183°.

B. Data selection

After following the standard calibration procedures for all CLAS detector elements the raw data were converted into a condensed format (DST) containing track and particle ID information. Quality checks ensured that malfunctioning detector components, changes in the target and/or potential sources of false asymmetries did not contaminate the data. DST files not meeting the minimal requirements outlined in [**?**] were eliminated from analysis.

Event selection criteria were applied to identify scattered electrons and minimize the background from other particles, primarily π^-. These criteria are based on the signals from the CC and the EC and are discussed in detail in [**?**]. We ascertained that the remaining π^- contamination of our electron sample was less than 1% over the whole kinematic range. The data were corrected for this remaining contamination by dividing out the "dilution" of the measured asymmetry by the pion contribution, with a systematic error assumed to be 100% of the (tiny) correction.

For the determination of the product of beam and target polarization ($P_b P_t$, see below) as well as kinematic corrections, we also required a sample of quasi-elastic $(e,e'p)$ events. We selected ep coincidences through a timing cut of ± 0.8 ns on the difference between the reconstructed electron and proton vertex time. Quasi-elastic events were selected through cuts on W, 0.89 GeV $\leq W \leq$ 1.01 GeV, missing energy (of the unobserved nuclear remnant) of ≤ 0.08 GeV (kinetic), and on the difference between the polar ($|\Delta\theta| \leq 2^\circ$) and azimuthal ($|\Delta\phi| \leq 3^\circ$) angles of the detected proton and the reconstructed direction of the virtual photon. These cuts were optimized to include most of the ep coincidences from quasi elastic scattering on the deuteron, while the contribution from the other target components (nitrogen, ^{4}He and foils) was much suppressed due to the wider nucleon momentum distributions in these nuclei, see Fig. 2

C. Event corrections

The track information for particles in the DSTs is based on an "ideal" detector and has to be corrected for various effects from detector materials and imperfections. Among other corrections, energy loss due to ionization in the target (both for the incoming and the scattered electron), multiple scattering angle deviations (compared to the average vertex of all particles in an event), and known deviations of the target magnetic field from the ideal version implemented in the reconstruction software were corrected for on an event-by-event basis.

The reconstruction software also assumes that a track originates on the nominal central axis ($x = y = 0$) of CLAS. In reality, the beam is rastered over a diameter of about 1.5 cm around that axis, and typically offset by a few mm. Since the raster position can be inferred from the currents in the raster magnets, the reconstructed vertex can (and has been) corrected for this offset.

The position and orientation of the drift chambers in space and the detailed three-dimensional shape of the torus magnetic field are not known with absolute precision; an empirical parametrization of their deviations from the "ideal" detector was fitted to fully exclusive events, using four-momentum conservation. This parametrized correction for particle momenta and scattering angles was also applied to each track. The resulting improvement of the resolution in the missing mass W (for the example of scattering off a NH_3 target) is shown in Fig. 3

A final correction was applied to the integrated beam charge measured by the Faraday Cup, to account for beam loss between the target and the FC due to multiple scattering and over-focusing in the target field.

D. From raw to physics asymmetries

For each combination of beam energy, torus polarity and target polarization, electron tracks were sorted by kinematic bins and were counted separately for positive (N^+) and negative (N^-) beam helicity, where "+" refers to a beam helicity antiparallel to the direction of the target polarization. These counts were normalized to the corresponding integrated Faraday charges, $n^\pm = N^\pm / FC^\pm$. Only events coming from complete pairs of "beam buckets" with opposite helicity were counted to avoid false asymmetries; we also ascertained that, after averaging over all target polarizations, the residual beam charge asymmetry $(FC^+ - FC^-)/(FC^+ + FC^-)$ was less than 10^{-4}. These normalized counts were used to form the raw asymmetry

$$A_{raw} = \frac{n^+ - n^-}{n^+ + n^-} \tag{21}$$

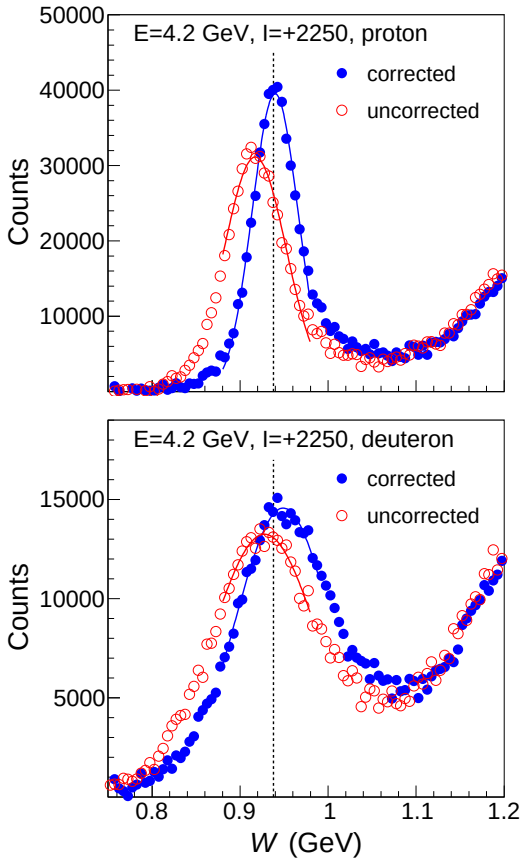

FIG. 3: Missing mass W before (red-hallow) and after (blue-solid) the kinematic corrections for the 4.238+ data set for NH_3 (top) and ND_3 (bottom) targets. The corrections decreased the distribution width and centered the mean value on the 0.938 GeV proton mass.

in each kinematic bin. This raw asymmetry was then converted to the desired physics asymmetry $A_{||}$ (Eq. 6) by applying a series of corrections which we now discuss in sequence.

1. *Dilution factor*

The dilution factor $F_{DF} \equiv n_d/n_A$ is defined as the ratio of events from polarizable nuclei of interest (here, deuterons bound in ammonia, n_d) to those from all components of the full ammonia target (n_A). It is calculated directly from radiated cross-sections on all components of the target. In terms of densities (ρ), material thicknesses (ℓ) and cross-sections per nucleon (σ),

$$n_d \propto \frac{6}{21}\rho_A \ell_A \sigma_d \tag{22}$$

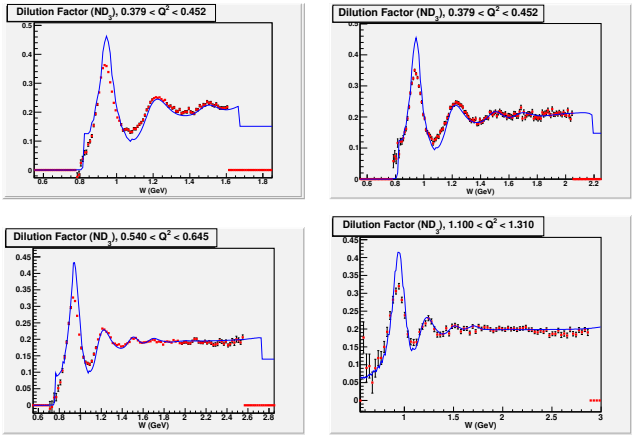

FIG. 4: Dilution factors as a function of W, shown at four different beam energies (1.6+ (top left), 2.5− (top right), 4.2− (bottom left) and 5.7− (bottom right)). The results from our standard method (using cross section models) are shown as blue lines, with the results from the data-based method shown as the red data points.

$$n_A \propto \rho_{Al}\ell_{Al}\sigma_{Al} + \rho_K \ell_K \sigma_K + \rho_A \ell_A (\frac{6}{21}\sigma_d + \frac{15}{21}\sigma_N) + \rho_{He}(L - \ell_A)\sigma_{He} \tag{23}$$

with the subscripts A, Al, K, N, and He denoting deuterated ammonia ($^{15}ND_3$), aluminum foil, kapton foil, nitrogen (^{15}N) and helium (^4He), respectively. The acceptance-dependent proportionality constant is identical in both of the above relations for a given kinematic bin. Inclusive scattering data from the empty (LHe) and ^{12}C targets were analyzed to determine the total target cell length (L) and effective ND_3 thickness (ℓ_A) using similar equations.

The required cross-sections were calculated from a fit to world data for F_1 and F_2 for protons and neutrons, using a Fermi-convolution model to fit inclusive scattering data on nuclear targets, including EG1b data from ^{12}C, solid ^{15}N and empty (LHe) targets [**?** **?**]. The nuclear EMC effect was parametrized using SLAC data [**?**]. Radiative corrections used the treatment of Mo and Tsai [**?**]; external Brehmsstrahlung probabilities incorporated all material thicknesses in CLAS from the target vertex through the inner layer DC.

Dilution factors F_{DF} were calculated for each data set and used to correct the raw asymmetry,

$$A_{undil} = \frac{A_{raw}}{F_{DF}}, \tag{24}$$

to get the undiluted asymmetry due to deuterons in the target. We checked our results for F_{DF} against an older data-based method [**?**][**?**][**?**] that uses the measured counts from three different targets and a simple model of neutron/proton cross-section ratios to express the background in the ammonia target in terms of the counts from carbon and empty targets. Values of L and ℓ_A varied by less than 2% between the two methods. Figure 4 shows the

result from both methods for four different examples. For the inelastic data, $W > 1.1$ GeV, the dilution factor from the cross-section based method were more precise and were used to correct the raw asymmetries. We used the data-driven method only in the quasi-elastic region $W < 1.08$ GeV (for the determination of beam and target polarization in one case, see below) and to subtract the background from exclusive $d(e,'ep)n$ events (see Fig. 2). This is because finite detector resolution effects (which are not included in the cross section model) affect the shape of sharply peaked spectra in the quasi-elastic region significantly, making the data-driven method more reliable.

The densities and thicknesses of all target materials were varied within their known tolerances to determine systematic uncertainty effects; only the variations of $\rho_C \ell_C$ and ρ_{He} had any significant (>1%) effect on F_{DF}. Uncertainties due to the cross-section model were estimated by the comparison of F_{DF} to a third-degree polynomial fit to the data-based dilution factors determined by the alternate method.

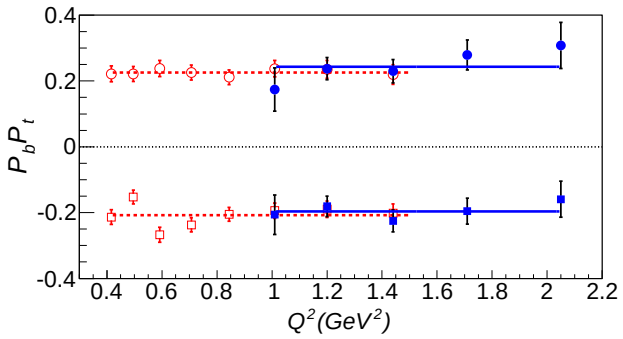

FIG. 5: P_bP_t values for the 2.5 GeV inbending data sets. The plot shows the resulting P_bP_t values for the Q^2 bins with available data. The results from the exclusive (blue square) and the inclusive (brown circle) methods are shown. The corresponding linear fits to the data are also shown as lines: the solid blue line is for the exclusive and the dashed brown line is for the inclusive methods.

2. *Beam and target polarizations (P_bP_t)*

The second major factor to consider when extracting the physics asymmetry $A_{||}$ is the product of beam and target polarization by which the measured asymmetry must be divided.

Because NMR measurements provided accurate target polarization measurements only near the edge of the target cell [**?**] (which was not uniformly exposed to the beam), we determined the polarization product P_bP_t directly from our data, using quasi-elastic $d(e,e'p)n$ and (in one case) $d(e,e')$ events. Here, we made use of the fact that the theoretical asymmetry in this case depends only on the electromagnetic form factors of proton (and neutron), see Section II E, which are well-known [**?**], giving us reliable predictions of $A_{||}$. After correcting for the (relatively smaller) dilution of this asymmetry from non-deuterium components of the target, we can directly divide the measured $A_{||}$ by the theoretical one to extract P_bP_t:

$$P_bP_t = \frac{A_{meas}^{quasi-el}}{F_D\ A_{theo}^{quasi-el}}. \qquad (25)$$

We used inclusive quasi-elastic events only in one case, for the 1.6 -1.7 GeV outbending configuration runs. In that case, too few of the protons from $d(e,e'p)n$ were detected in CLAS for a reliable determination of P_bP_t. We used a cut of 0.89 GeV $\leq W \leq$ 1.01 GeV to define quasi-elastic events. While this method yields a smaller statistical error, it has greater uncertainty because of larger background contributions; therefore, a systematic error of 10% was assigned to these particular P_bP_t values.

For all other configurations, we used exclusive $d(e,e'p)n$ events within the cuts listed in Section IV B which have very little background from nuclear target components (see Fig. 2). We used a detailed Monte Carlo simulation, including Fermi motion of the proton inside the deuteron, to calculate the theoretical asymmetry. For both methods, the nuclear background was determined using the data-driven method mentioned in Section IV D 1. We compared the results to the values derived from inclusive quasi-elastic scattering in all cases, and found them generally to be consistent within the statistical error.

The derived P_bP_t values were checked for consistency across Q^2 for each beam energy, torus current and target polarization direction. Sample P_bP_t values across Q^2 for 2 beam energies are shown in Figure 5. P_bP_t values ranged from a low of 0.1 to 0.28, with most values between 0.15 and 0.25. We varied each of the values of P_bP_t individually by the larger of one (statistical) standard deviation and its difference to the inclusive result to assess the systematic uncertainty of all physics quantities due to P_bP_t.

3. *Polarized nitrogen and target contamination corrections*

Apart from the *dilution* of the measured asymmetry by nucleons embedded in nitrogen, helium and other target materials (Section IV D 1), one has to consider further small modifications of this asymmetry due to polarized target nucleons outside of deuterium.

First, it is well-known that the ^{15}N nuclei in the ammonia molecules become somewhat polarized as well. EST (Equal Spin Temperature) theory predicts the polarization ratio between two spin-interacting nuclear species in a homogenous medium as the ratio of their magnetic moments [**?**]: $P_{^{15}N}/P_{^2H} \approx \mu_{^{15}N}/\mu_{^2H} \approx -0.4 \cdots -0.5$. Using a simple shell model description [**?**] of the ^{15}N nucleus, this polarization is carried by a single proton in the $1p_{1/2}$ shell, which means that this proton is spin-polarized to -33% of the overall nucleus. The measured magnetic moment of ^{15}N suggests a somewhat smaller spin polarization, so that the overall contribution from nitrogen to the measured asymmetry can be approximated by that of a

bound proton with $P_p^{bound} = 8\% \ldots 16\%$ of the deuteron polarization. Accordingly, we subtracted a correction of $1/3 \times P_p^{bound} \times A_p \sigma_p^{bound}/\sigma_d \approx 0.013 \ldots 0.04 A_p$ from the measured asymmetry, where the factor $1/3$ accounts for the fact that there are three deuteron nuclei per nitrogen nucleus in ammonia.

A second contamination to the measured asymmetry comes from isotopic impurities of the deuterated ammonia, with some deuterons replaced by protons. Typical contaminations quoted in the literature [**?**] are around 1.5%. We did a careful study [**?**] that showed a ^{1}H contamination of up to about 3.5% during EG1 (which was included in the dilution factor); however, that same study put an upper limit of 2% on the fraction of these extra protons that were polarized (the remainder are presumably bound in molecules like H_2O and are unpolarized). The degree of polarization of these protons can be estimated as $P_p/P_d \approx 1.2...1.5$, again according to EST and empirical evidence [**?**]. The net effect is an additional term proportional to A_p that has to be subtracted from the measured asymmetry. The total correction for bound and free polarized protons in the target is $0.027 \ldots 0.051 A_p$. We took the median of this range to correct our data (using a model of the asymmetry A_p based on our proton results [**?**]) and $1/2$ of its spread to estimate systematic uncertainties. An additional correction due to the very small contribution of ^{14}N nuclei (less than 2% of our ammonia sample) was too small to be applied but was included in the overall systematic uncertainty.

Quasi-elastic $d(e,e'p)n$ events are also affected by the various target contaminations discussed above. We applied a corresponding correction to our extraction of $P_b P_t$ (Section IV D 2).

4. Other background subtractions

Dalitz decay of neutral pions [**?**] and Bethe-Heitler processes [**?**] can produce e^+e^- pairs at or near the vertex, contaminating the inclusive e^- spectrum. This contamination was at most a few percent of the data rate (at high W) and was measured by comparing positron and electron rates for runs with opposite torus polarity. We also measured the positron asymmetry and found it consistent with zero. We subtracted this background, using the measured rate and assuming zero asymmetry. To estimate the corresponding systematic error, we alternatively assumed a constant positron asymmetry consistent with the spread of values we measured, and varied the rate within its uncertainty. Details can be found in the companion paper on the proton [**?**].

There also was a tiny (sub-percent) remainder of the background from π^- misidentified as electrons, after all cuts.This background was subtracted in a similar way.

5. Radiative corrections

Radiative corrections to the measured asymmetries $A_{||}$ were computed using the program RCSLACPOL, which was developed at SLAC for the spin structure function experiment E143 [**?**]. Polarization-dependent internal and external corrections were calculated according to the prescriptions in Ref. [**?**] and Ref. [**?**], respectively.

We compared the calculated double spin asymmetry $A_{||}$ with radiative effects turned on, A_r, to the Born asymmetry A_B calculated with the same models (see Section V D). We determined parameters f_{RC} and A_{RC} for each kinematic bin, allowing us to write the Born asymmetry as

$$A_B = \frac{A_r}{f_{RC}} + A_{RC} \tag{26}$$

in which f_{RC} is a "radiative dilution factor" accounting for the count rate fraction from the elastic and quasi-elastic tail within a given bin. This correction was then applied to all data.

Systematic uncertainties on these corrections were estimated by running RCSLACPOL for a range of reasonable variations of the models for F_2, R, A_1 and A_2 (see Section V D) and for different target thicknesses and cell lengths, ℓ_A and L. The changes due to each variation where added in quadrature and the square root of this quantity taken as the systematic error on radiative effects.

6. Systematic uncertainties

Estimation of systematic uncertainties on each of the observables discussed in the following section was done by varying a particular input parameter, model or analysis method, rerunning the analysis, and recording the difference in output for each of the final asymmetries, structure functions and their moments. Final systematic uncertainties attributable to each altered quantity were then added in quadrature to estimate the total uncertainty. Note that for each quantity of interest (A_1, g_1, Γ_1) the systematic error was calculated by this same method (instead of propagating it from other quantities), therefore ensuring that all correlations in these errors were properly taken into account.

Systematic uncertainty	Typical range (in % of g_1/F_1)
Pion and e^+e^- contamination	0.04% – 1%
Dilution Factor	1.8% – 2.7%
Radiative corrections	3.5% – 5.7%
$P_b P_t$ uncertainty	5.9% – 22.4%
Model uncertainties	2.0% – 5.0%
Polarized Background	1.0% – 1.7%
Total	10% – 23%

TABLE I: Table of Systematic Error Magnitudes

Most sources of systematic uncertainties have been discussed above. These sources include kinematic shifts, bin averaging, target parameters (radiative corrections), nuclear dilution model, structure function models, $P_b P_t$ uncertainty

for each individual data set, and background contaminations. The relative magnitudes of these various contributions to the systematic error, for the example of the ratio g_1/F_1, are listed in Table I. The results shown in the next section incorporate these systematic errors.

V. RESULTS AND COMPARISON TO THEORY

A. Results for $A_1 + \eta A_2$

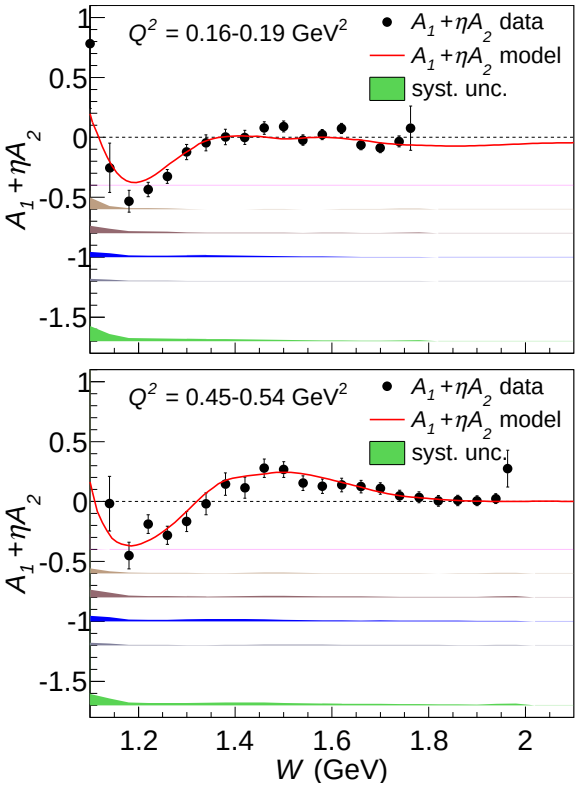

FIG. 6: (Color Online) Representative values for the double-spin asymmetry $A_1+\eta A_2$ versus final invariant mass W from the 1.6 and 2.5 GeV data sets. The top panel is for 0.16 $(\mathrm{GeV}/c)^2 \leq Q^2 \leq 0.19$ $(\mathrm{GeV}/c)^2$ and the bottom panel for 0.45 $(\mathrm{GeV}/c)^2 \leq Q^2 \leq 0.54$ $(\mathrm{GeV}/c)^2$. The red-solid line represents our model parametrization of $A_1+\eta A_2$. The shade at the bottom (green) is the total systematic error. The individual contributions are offset from the x-axis as follows, from top to bottom: pion and pair symmetric contamination (-0.4; barely visible); dilution factor (-0.6); $P_b P_t$ (-0.8); models plus radiative corrections (-1.0); polarized background (-1.2).

In this section, we present our final results for all quantities of interest: A_1, g_1 and moments for the deuteron and the neutron. As the first step, we divide the fully corrected Born asymmetry $A_{||}$ by the depolarization factor D (Eq. 8) to extract the combination $A_1+\eta A_2$ for each bin in W and Q^2 and each beam energy. Results for similar beam energies (e.g., 1.6 and 1.7 GeV) and inbending and outbending torus polarization are combined into averaged values for four "nominal" energies (1.6 GeV, 2.5 GeV, 4.2 GeV and 5.7 GeV), weighted by their statistical precision. We checked that in each case, the data sets that we combined agree with each other within statistical and systematic uncertainties. Figures 6 and 7 show the results for $A_1 + \eta A_2$ for selected Q^2 bins and for each of the four standard energies. The systematic errors from different contributing sources are also shown as shades at the bottom of each plot. For most kinematics, the largest contribution to the systematic error is due to the uncertainty in the beam and target polarization, with some contribution from dilution factor and radiative correction uncertainty. We note that our data for all 4 beam energies are well described by our model (see below) indicated by the red solid line.

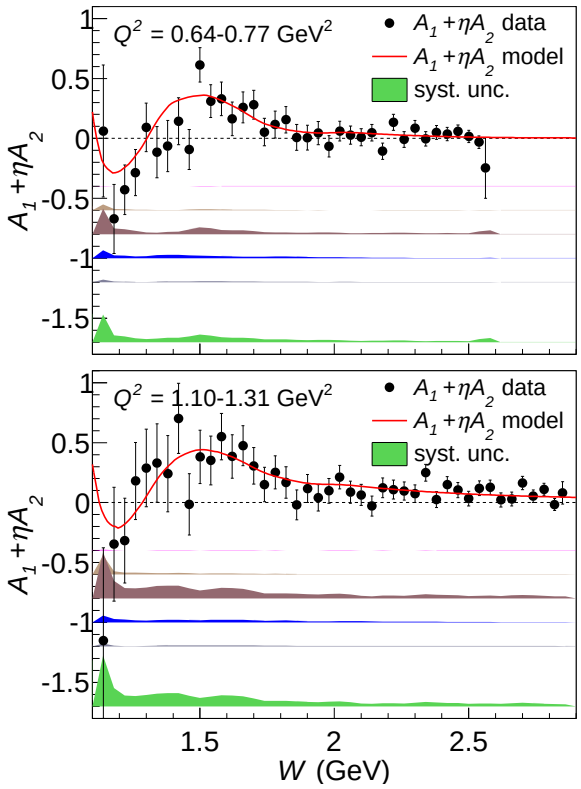

FIG. 7: Same as Fig. 6 except for 4.2 and 5.7 GeV beam energies. The top panel is for 0.64 $(\mathrm{GeV}/c)^2 \leq Q^2 \leq 0.77$ $(\mathrm{GeV}/c)^2$ and the bottom panel for 1.1 $(\mathrm{GeV}/c)^2 \leq Q^2 \leq 1.3$ $(\mathrm{GeV}/c)^2$.

B. The virtual photon Asymmetry A_1

Once $A_1 + \eta A_2$ is calculated, we can extract the virtual photon asymmetry A_1, by using model inputs for A_2 (see below). Since A_1 depends only on W and Q^2, we can combine the results from all beam energies at this stage, again weighted by statistical error. Figure 8 shows A_1 together with different sources of systematic errors. The error due to our uncertainty on A_2 is the dominant contribution to the

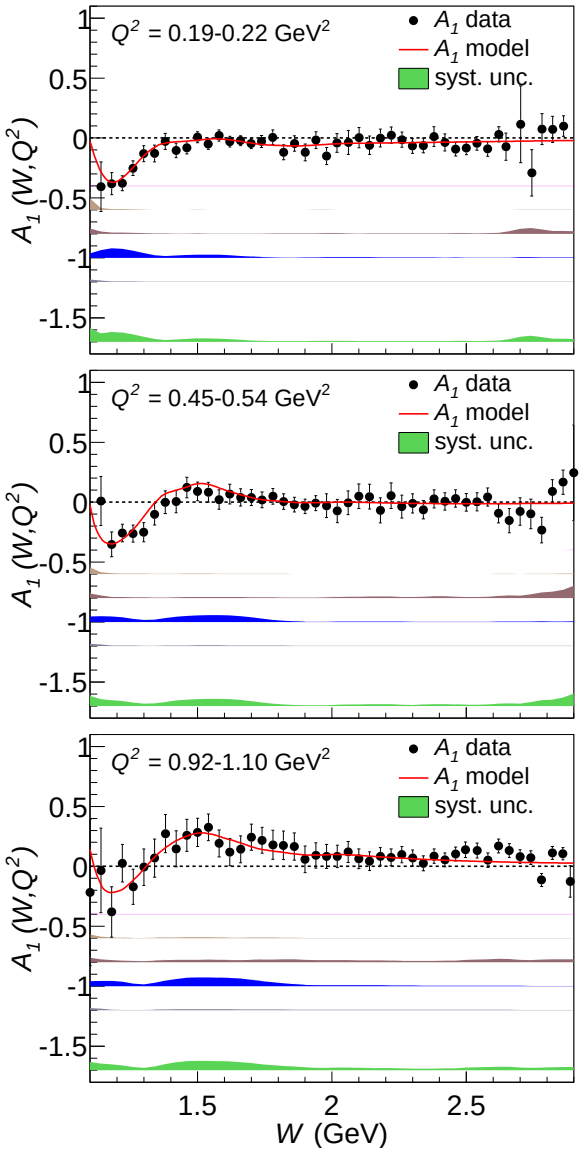

FIG. 8: (Color Online) Virtual photon asymmetry A_1 for the deuteron, versus W, for a few Q^2 bins: 0.16 $(\mathrm{GeV}/c)^2 \leq Q^2 \leq$ 0.19 $(\mathrm{GeV}/c)^2$ (top), 0.45 $(\mathrm{GeV}/c)^2 \leq Q^2 \leq 0.54$ $(\mathrm{GeV}/c)^2$ (middle) and 1.1 $(\mathrm{GeV}/c)^2 \leq Q^2 \leq 1.3$ $(\mathrm{GeV}/c)^2$ (bottom). The statistical uncertainties are indicated by error bars, while the total systematic errors are indicated by the shaded band at the bottom. Again, the individual contributions are shown separately as offset bands: pion and pair symmetric contamination (-0.4); dilution factor (-0.6); $P_b P_t$ (-0.8); models plus radiative corrections (-1.0); polarized background (-1.2).

shaded band representing "models".

In addition, Figs. 9 and 10 show the final A_1 versus final state invariant W mass for all Q^2 bins in our kinematic coverage. Gaps are due to lacking kinematic coverage between the different beam energies. Data points with very large statistical or systematic errors were omitted from these plots.

At all but the highest Q^2, the effect of the $P_{33}(1232)$

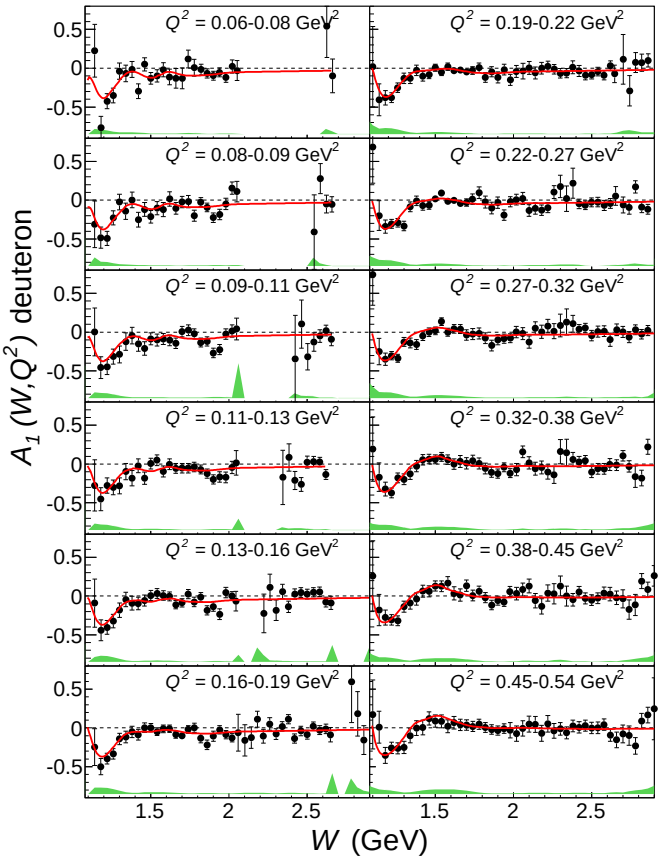

FIG. 9: (Color Online) A_1 for the deuteron versus the final state invariant mass W for various Q^2 bins. Total systematic errors are shown as shaded area at the bottom of each plot. Our parametrized model is also shown as a red line on each plot. Only the data points with $\sigma_{stat} < 0.3$ and $\sigma_{sys} < 0.2$ are plotted.

(Delta) resonance is clearly visible in the strongly negative values of A_1, due to the dominance of the $A_{3/2}$ transition to this resonance. At our lowest Q^2, the asymmetry is in general negative or close to zero, which proves that the $A_{3/2}$ transition amplitude is dominant in this region as expected from exclusive pion production. As we go to higher values of Q^2 and W, the transition amplitude $A_{1/2}$ leading to resonances such as $D_{13}(1520)$ and $S_{11}(1535)$ becomes dominant, as expected from pQCD. At $W > 2$ and larger Q^2, the asymmetry continues smoothly from the resonance region into the DIS region where it has been measured by previous experiments to be positive, due to the larger contribution from the proton (with $A_1 > 0$ throughout the measured x range in the DIS region).

This trend becomes more apparent if we integrate our data on A_1 over the full measured DIS range with $W > 2$ GeV and $Q^2 > 1.1$ $(\mathrm{GeV}/c)^2$ and plot it as a function of the scaling variable x. The behavior of $A_1(x)$ at large x is of high interest to test various models inspired by QCD, as outlined in Section II C. Figure 18 shows this quantity from EG1b together with world data and various models. [TO BE

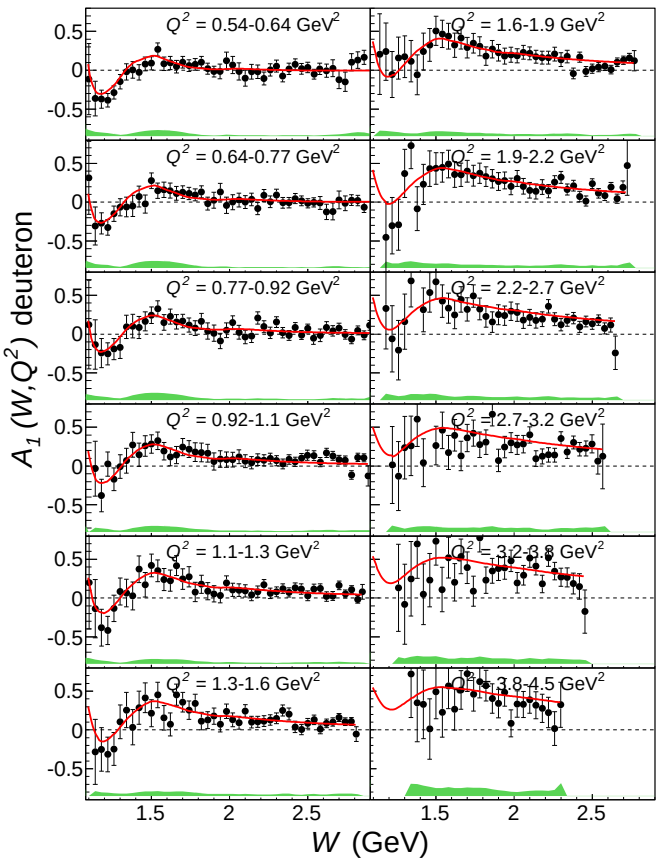

FIG. 10: Continuation of Fig. 9 for remaining Q^2 bins.

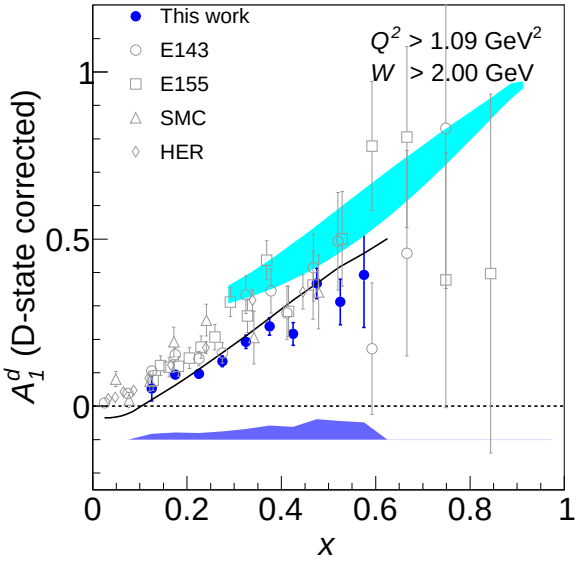

FIG. 11: (Color Online) A_1^d versus x_{Bj} in the DIS region from EG1b and other experiments. Statistical uncertainties are indicated by error bars, and EG1b systematic uncertainties by the shaded band.

AUGMENTED] We note that while our data appear to lie below most of the other world data, they agree reasonably well with our model (see below) which was calculated at the average kinematics of each data point. This model, in turn, describes the world data well; therefore, we conclude that A_1 has a non-negligible Q^2 dependence even in the DIS region, since our data are at significantly lower average Q^2 than those from other experiments.With this caveat, they are in reasonable agreement with the expectation of a continued rise at high x (as indicated, e.g., by the model of N. Isgur), but not with as rapid a rise as predicted by pQCD.

C. The spin structure function g_1

In addition to extracting A_1, we can also use the measured asymmetry $A_{||}$ to extract the spin structure function g_1^d according to Eq. 9. For this purpose, we use models for the unpolarized structure function F_1 and for A_2 (see next section). The results for g_1^d versus Bjorken x for each of our Q^2 bins are presented in Figs. 12 and **??**. The red curve on each plot comes from our model. At low Q^2, g_1 is strongly affected by resonance structures, in particular again the $P_{33}(1232)$ being the most prominent one, making g_1 negative in this region. When we go to higher Q^2, the effect of the resonances diminishes and g_1 approaches the smooth DIS curve also shown in Figs. 12 and **??** as blue dashed line. This can be interpreted as a sign that quark-hadron duality begins to work at these larger $Q^2 > 1.0$ (GeV/c)^2. However, in the $P_{33}(1232)$ region, the data falls noticeably below the blue line even at rather high Q^2.

One feature to notice is that $g_1(x)$ appears to rise again towards $x = 1$, in marked contrast to the proton case. This is an artifact due to the quasi-elastic contribution (pn breakup of the deuteron) which is strong and positive at small Q^2; see also Section II E.

In the DIS region ($W > 2$ GeV and $Q^2 > 1$ GeV$^2/c^2$), $g_1^d(x)$ can be used to extract information on the quark helicity contributions to the nucleon spin (see Section II D). Comparing our data to the higher Q^2 data from COMPASS **??** one can extract information on the gluon polarization through DGLAP evolution. Including our data for somewhat lower Q^2, higher twist modifications of the polarized PDFs can be constrained. Our data are available for such PDF fits, including the recent fit by the JAM collaboration [**?**], as well as for more rigorous tests of duality

D. Models

To extract the physics quantities discussed above from our data on $A_{||}$, we require models both for the unpolarized structure functions F_1 and F_2 (or, equivalently, F_1 and R), as well as for the asymmetry A_2. These models (plus a model for the asymmetry A_1) are also needed to evaluate radiative corrections (Section IV D 5) and to extrapolate our

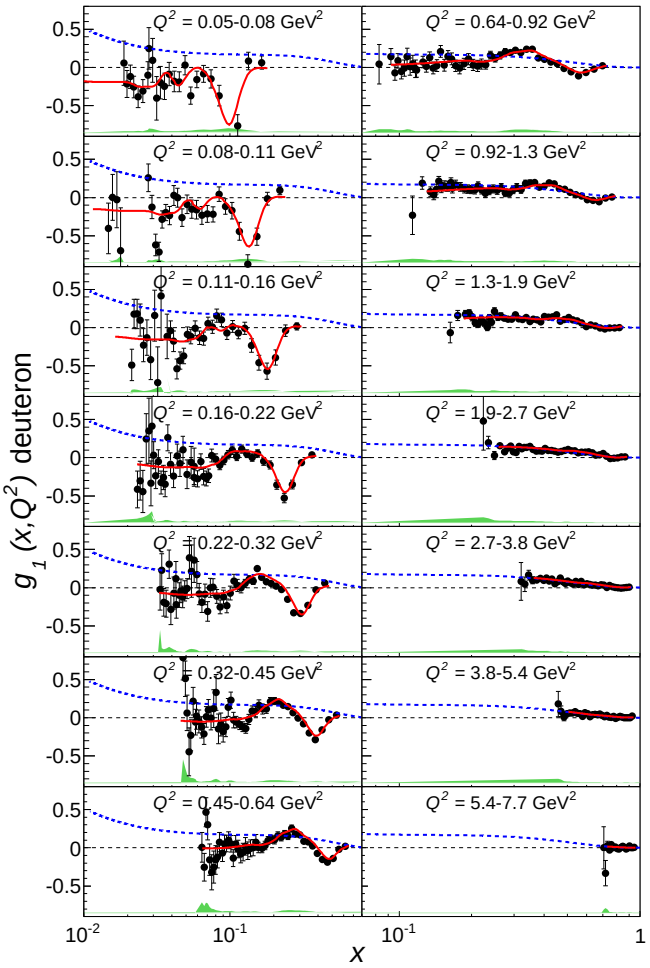

FIG. 12: (Color Online) g_1 versus the Bjorken variable x for the lower Q^2 bins, together with our model shown as red line on each plot. The shaded area at the bottom of each plot represents the systematic error. The corresponding DIS parametrization for $Q^2 = 10$ GeV is also shown as blue dashed line.

data to small x, for the purpose of evaluating moments of g_1 (see next section). For the deuteron case in particular, we need models for both the proton and the neutron as well as a prescription for "Fermi-smearing" and combining them.

We describe our fit in detail in Ref. [**?**]. Our approach to Fermi-smearing is explained in Section II G. Here, we just summarize our sources of data for the fits to A_2 and A_1 for the proton and the neutron. For the unpolarized structure functions $F_1^{p,n}$ and $R^{p,n}$, we used a recent parametrization of the world data by Bosted and Christy [**?** **?**]. This parametrization fits both DIS and resonance region data with an average precision of 2-5%, including Hall C data on the proton and the deuteron with very similar kinematics to ours. Systematic errors due to uncertainties in these models where calculated by varying either F_1 or R by the average uncertainty of the fit and recalculating all quantities of interest.

For the asymmetries in the region $W > 2$ GeV, we developed our own phenomenological fit to the world data, including all DIS results from SLAC, HERA and CERN and from Jefferson Lab data (see Ref. [**?**] for a complete list). In the resonance region, we added data from EG1a [**?** **?**] in Hall B, RSS [**?**] in Hall C and MIT-Bates [**?**]. We also used the data reported here and in [**?**] and iterated the fit after re-extracting them using the updated models. The proton asymmetries were fit first, followed by a fit to the neutron A_1 and A_2. For this second part, we used the rich data set collected on ^{3}He in Jefferson Lab's Hall A [**?**], at SLAC [**?** **?**] and at HERMES [**?**], as well as data on the deuteron. The goodness (χ^2) of the fit was calculated by comparing the fit functions for neutron asymmetries directly with neutron results extracted from ^{3}He data, as well as the convolution of our proton and neutron models with the deuteron momentum distribution. To anchor our fit of A_1 at the photon point, we used data from ELSA and MAMI (see, e.g., the summary by Helbing [**?**]). As a result, we achieved a consistent fit of proton, deuteron and neutron data over a wide kinematic range, far exceeding our own kinematic coverage.

Our fit results are shown as curves on most of the plots in this section and are generally in very good agreement with the existing data (including our own). We developed alternative model fits representing the uncertainty of our fit results in all cases and estimated the systematic errors on all extracted quantities due to model uncertainties by replacing the "standard fits", one by one, with these alternatives.

E. Moments of g_1

In the following, we discuss various moments of spin structure functions that can be determined from our data. We evaluate those moments for each of our standard Q^2 bins in two parts. For W regions where we have good data (with statistical errors not much larger than average), we sum directly over these data (binned in 10 MeV bins in W), multiplied by the corresponding bin width in x and the required power of x. We avoid the region below $W = 1.15$ where radiative effects and the quasi elastic contribution overwhelm the data. The upper end of the integration range depends on the Q^2 bin and can go up to $W = 3$ GeV. The resulting values of the integral are shown as the open (magenta) points in Fig. 13, and the systematic error (which is properly propagated as explained in the previous section) is shown as the lower (magenta) band. Note that all moments are calculated "per nucleon" (i.e., divided by 2 for the two nucleons in deuterium), following common practice. However, we do *not* correct for the deuteron D-state or any other nuclear effects.

We integrate our model for g_1 to add the small contribution from the region $W_{min} = 1.08$ GeV $\leq W \leq 1.15$ GeV. We exclude the (quasi-)elastic region $W < 1.08$, following common convention, since the quasi-elastic peak would overwhelm the integrals at small Q^2. Occasional, there are gaps in our W coverage from different beam energies, espe-

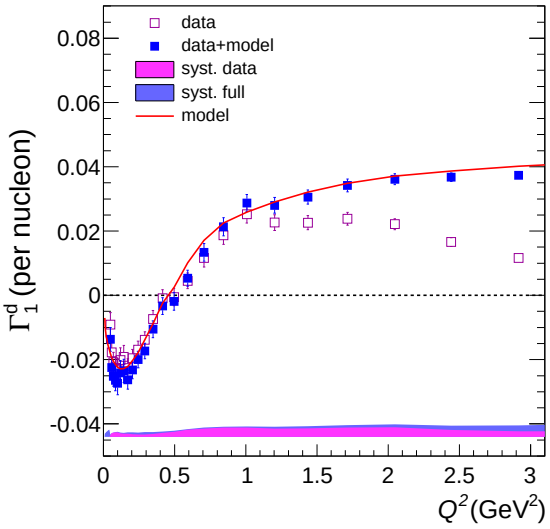

FIG. 13: (Color Online) Γ_1^1 for the deuteron versus Q^2 from data only (hollow-magenta squares) and data+model (full-blue squares), including the extrapolation to the unmeasured kinematics. The red curve is evaluated by only using the model. The systematic uncertainty is shown at the bottom of the plot, for data only (magenta shade) and data+model (blue shade).

cially at low Q^2 (see, e.g., Fig. 9). These gaps are also filled by integrating the model instead. Finally, we integrate the model from the lower x limit of our highest W bin (for each Q^2) down to $x = 0.001$. This contribution becomes most important at high Q^2 and for the lowest (first) moment. We limit ourselves to this minimum x value because there are practically no reliable data at lower x and our model becomes unconstrained and rather uncertain. While it is likely that there is no significant contribution below $x = 0.001$, we prefer to quote our results as moments from $x = 0.001$ to x_{max} where

$$x_{max} = \frac{Q^2}{W^2_{min} - M^2 + Q^2}. \qquad (27)$$

(The contribution from $x < 0.001$ is most certainly negligible for the higher moments.) The values of the full integral for the first moment are shown in Fig. 13 as the filled (blue) data points and the integral of the model over the same region is shown as the red curve. The full systematic error due to the additional model uncertainty in the unmeasured region is indicated by the wider blue band behind the magenta one.

Figure 14 shows the Q^2 evolution of the first moment as measured by the EG1b experiment (plus model extrapolation) and also selected world data on this quantity. We compare our results to our own model (solid red curve), the extrapolation from the DIS limit using pQCD corrections up to third order in α_s (black dotted curve), and two phenomenological fits from Burkert *et al.* [**?**] (short-dashed magenta curve) and Soffer *et al.* [**?**] (dot-dashed green curve). We also show several predictions for the low–Q^2

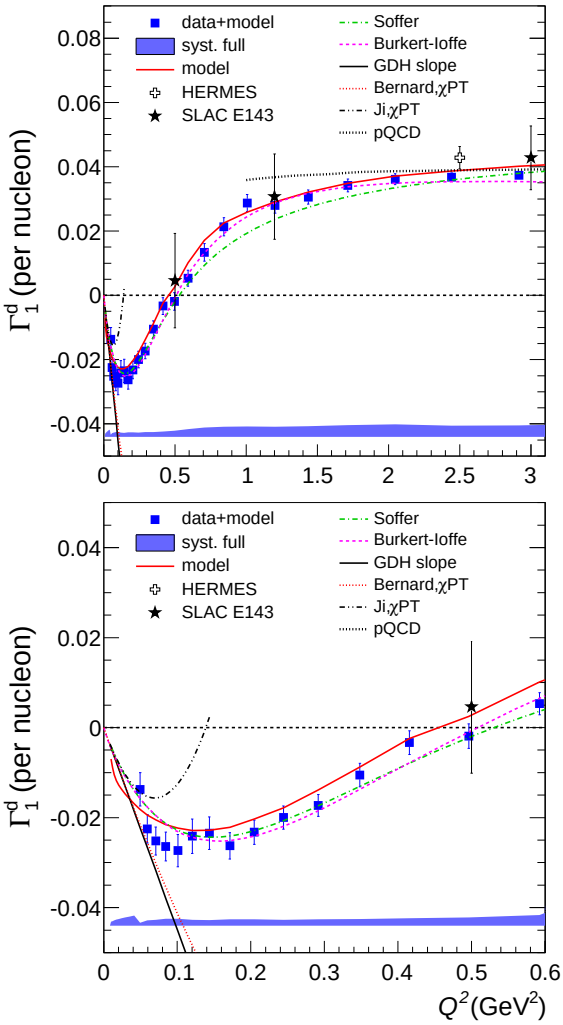

FIG. 14: Γ_1^1 for the deuteron versus Q^2 from our data with the model contribution from the unmeasured region $x \geq 0.001$ added in. The top plot is the same as Fig. 13 while the lower plot is zoomed into the low Q^2 region. Results from other experiments are also shown, including E143 [**?**], HERMES [**?**]. Curves are explained in the text.

behavior of $\Gamma_!$ (better visible in the lower panel of Fig. 14), including the slope at $Q^2 = 0$ from the GDH sum rule [**?**] and its extensions from two different chiral perturbation theory approaches: those by Ji [**?**] (grey dash-double dot) and by Bernard *et al.* [**?**] (red dotted). ADD MORE DISCUSSION LATER. UPDATE BERNARD. Basic points to make: The phenomenological curves work well; the ChPt curves make only contact at the lowest Q2.

The higher moments Γ_1^3 and Γ_1^5 are also calculated in the same way by using Eq. (**??**) with appropriate powers $n = 3, 5$. Fig. 15 shows the results for the third moment Γ_1^3 and the fifth moment Γ_1^5 of g_1 as extracted from the EG1b data. ADD DISCUSSION Mention that Gamma3 is connected to a2.

To calculate the extended spin polarizability γ_0 , we integrate the product of A_1F_1 instead of g_1, weighted with

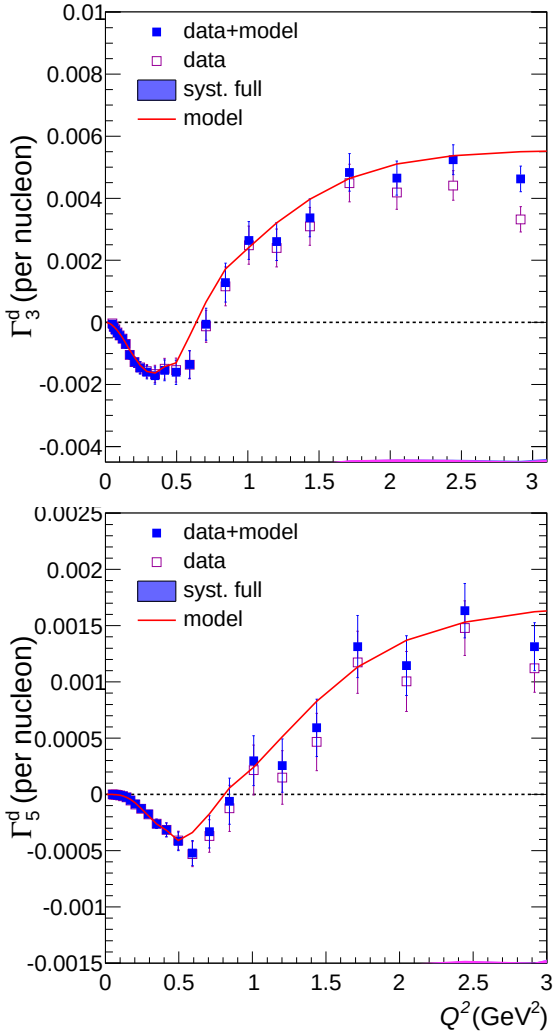

FIG. 15: Higher moments of g_1 extracted from the EG1b data are shown with respect to Q^2, the third moment Γ_1^3 (top), and the fifth moment Γ_1^5 (bottom). The hollow squares were calculated with no model contribution while the filled squares have model input for the kinematic regions with no available data.

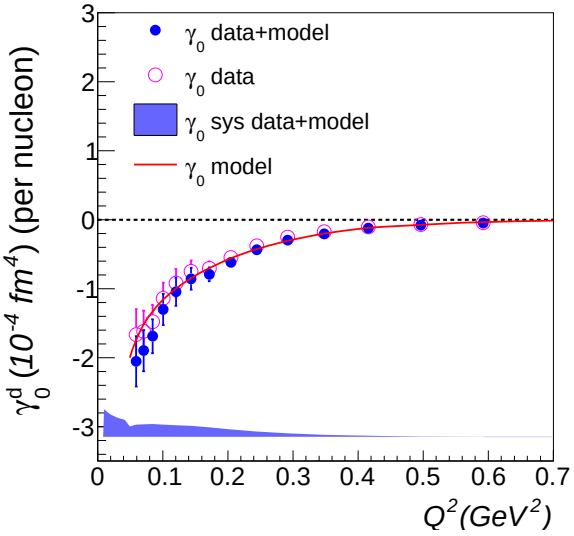

FIG. 16: Forward spin polarizability (γ_0) for the deuteron is shown versus Q^2. The hollow circles represent the calculation by using only data and the full circles are data + model results. The green shaded area is the total systematic error. The systematic error that comes from g_2, by taking $g_2 = 0$, is shown with the gray shade overlapped on the total systematic error. The model curve is also shown as a line through data points. The top plot shows values also multiplied by 15.134 for unit conversion to [10^{-4} fm^4]. The bottom plot is just the integral part, without the kinematic factor taken into account.

x^2. The result is multiplied with $16M^2(\hbar c)^4\alpha/Q^6$ to convert to [10^{-4} fm^4], in agreement with the definition for real photons. Fig. 16 shows our result for the forward spin polarizability γ_0 for the deuteron. ADD BERNARD CURVE. ADD MORE DISCUSSION

F. Neutron spin structure functions

Describe how we extracted the neutron from the deuteron. First time ever!

XXX

XXXX

****** SOME TEXT TO PREVENT FLOAT ERROR SOME TEXT TO PREVENT FLOAT ERROR SOME TEXT TO PREVENT FLOAT ERROR SOME TEXT TO PREVENT FLOAT ERROR SOME TEXT TO PREVENT FLOAT ERROR SOME TEXT TO PREVENT FLOAT ERROR ****************

****** SOME TEXT TO PREVENT FLOAT ERROR SOME TEXT TO PREVENT FLOAT ERROR SOME TEXT TO PREVENT FLOAT ERROR SOME TEXT TO PREVENT FLOAT ERROR SOME TEXT TO PREVENT FLOAT ERROR ****************

****** SOME TEXT TO PREVENT FLOAT ERROR SOME TEXT TO PREVENT FLOAT ERROR SOME TEXT TO PREVENT FLOAT ERROR SOME TEXT TO PREVENT FLOAT ERROR SOME TEXT TO PREVENT FLOAT ERROR ****************

****** SOME TEXT TO PREVENT FLOAT ERROR SOME TEXT TO PREVENT FLOAT ERROR SOME TEXT TO PREVENT FLOAT ERROR SOME TEXT TO PREVENT FLOAT ERROR SOME TEXT TO PREVENT FLOAT ERROR ****************

****** SOME TEXT TO PREVENT FLOAT ERROR SOME TEXT TO PREVENT FLOAT ERROR SOME TEXT TO PREVENT FLOAT ERROR SOME TEXT TO PREVENT FLOAT ERROR SOME TEXT TO PREVENT

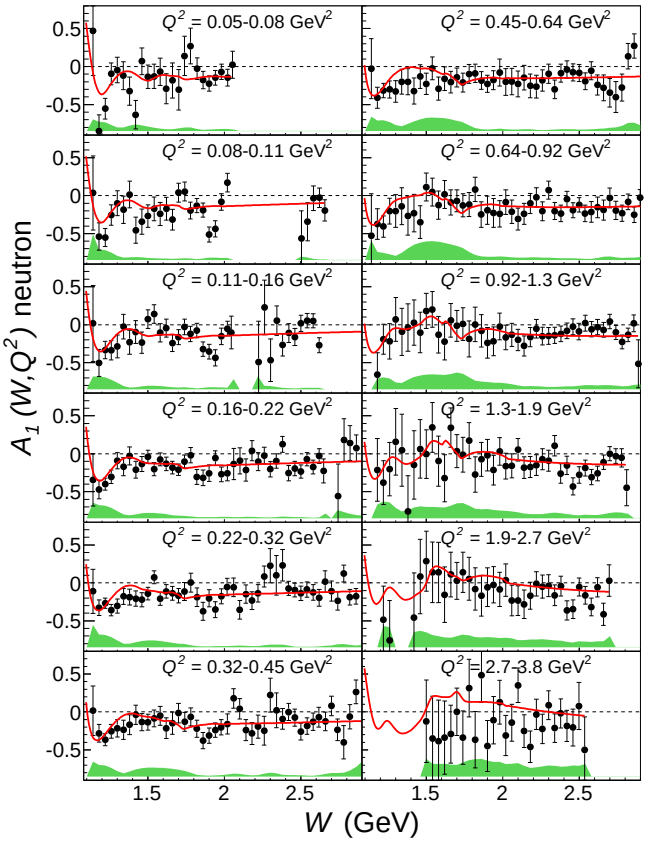

FIG. 17: A_1 for the neutron versus the final state invariant mass W for various Q^2 bins. Systematic errors are shown as shaded area at the bottom of each plot. Our parametrized model is also shown as a red line on each plot. Only the data points with $\sigma_{stat} < 0.3$ and $\sigma_{sys} < 0.2$ are plotted.

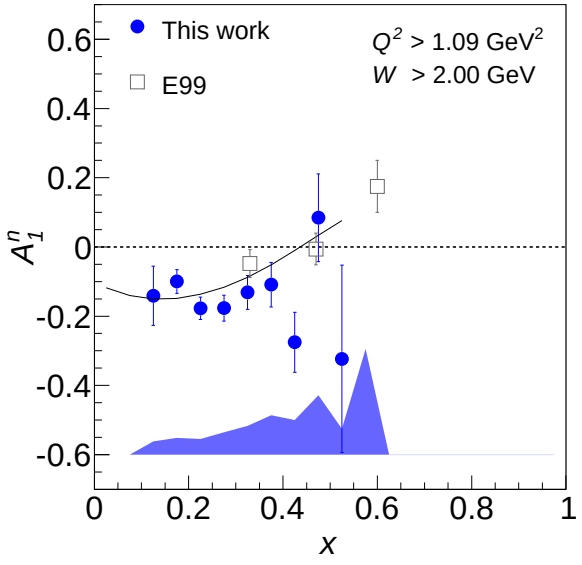

FIG. 18: A_1^n versus x_{Bj}.

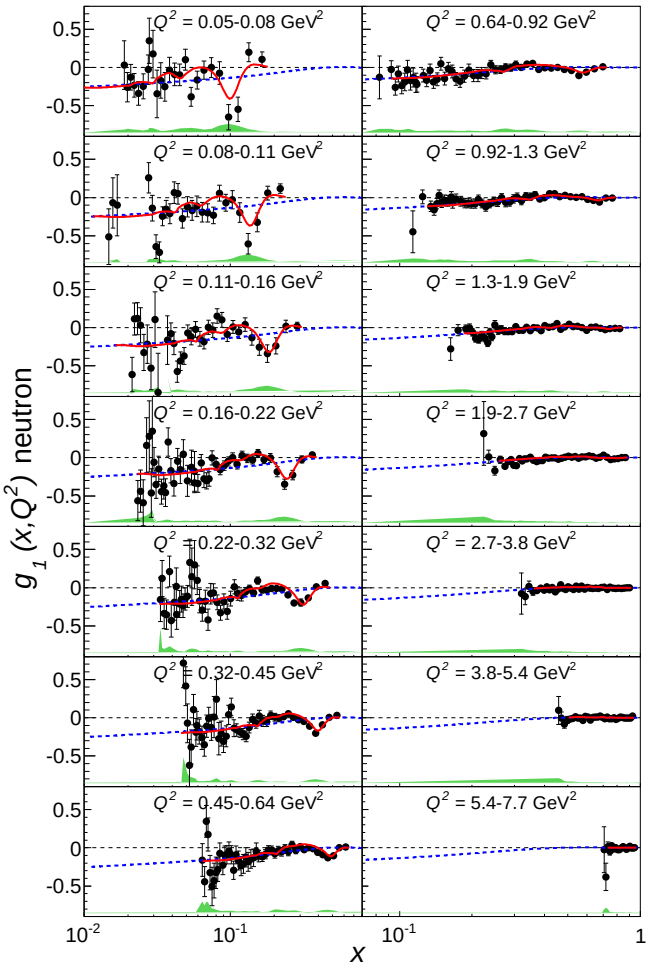

FIG. 19: g_1 for the neutron with respect to the Bjorken variable x for many Q^2 bins together with model shown as red lines on each plot. The shaded area at the bottom of each plot represents the systematic error. DIS curve for $Q^2 = 10$ GeV is also shown as blue dashed line.

FLOAT ERROR **********
****** SOME TEXT TO PREVENT FLOAT ERROR SOME TEXT TO PREVENT FLOAT ERROR SOME TEXT TO PREVENT FLOAT ERROR SOME TEXT TO PREVENT FLOAT ERROR SOME TEXT TO PREVENT FLOAT ERROR **********

VI. CONCLUSION

In summary, we present the final analysis of the most extensive and precise data set on the spin structure functions A_1 and g_1 of the deuteron. The data cover two decades in squared momentum transfer, $0.05 \leq Q^2 \leq 5$ GeV^2, connecting the region of hadronic degrees of freedom and effective theories like χPT near the photon point with the regime where pQCD is applicable. Our data give more detailed insight in the inclusive response of the deuteron in the

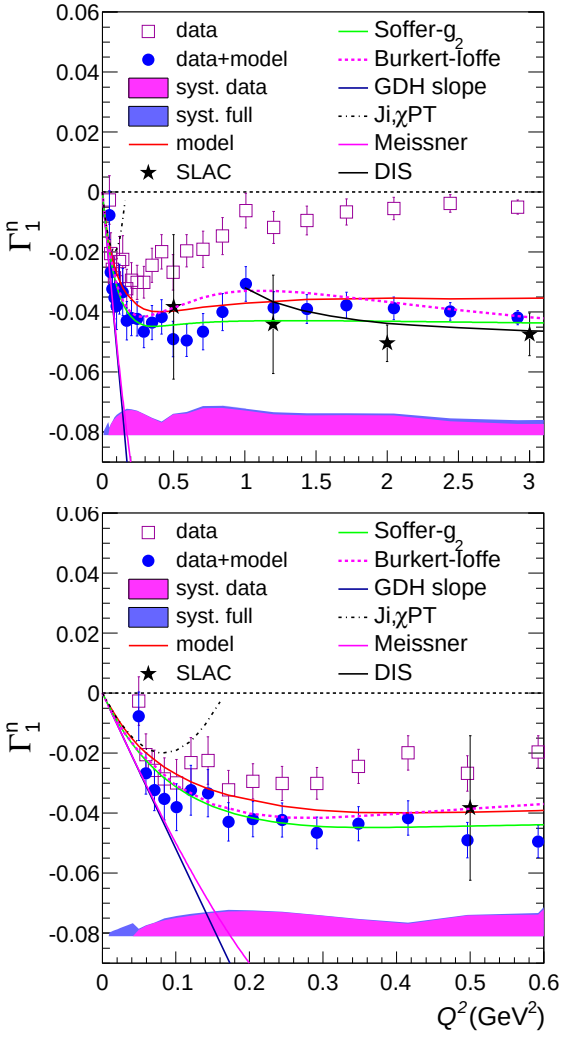

FIG. 20:
Γ_1^1 for the neutron versus Q^2 from data only (hollow-magenta squares) and data+model (full-blue squares), including the extrapolation to the unmeasured kinematics. The red curve is evaluated by only using the model. Also shown are phenomenological calculations from Soffer-Teryaev and Burkert-Ioffe, together with the χPT results from Ji [**?**] (black dotted dashed line) and Bernard [**?**] (red dotted line). The GDH slope (black solid line) and pQCD prediction (black dotted line) are also shown on the plots . The systematic errors are shown for only data (magenta shade) and data+model (blue shade) at the bottom of the plot. The bottom plot is the same only zoomed into the low Q^2 region. Results from other experiments are also shown.

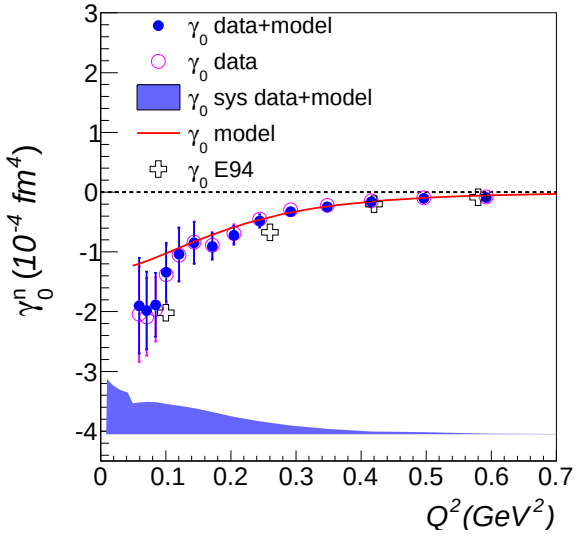

FIG. 21: Forward spin polarizability (γ_0) for the neutron is shown versus Q^2. The hollow circles represent the calculation by using only data and the full circles are data + model results. The green shaded area is the total systematic error. The systematic error that comes from g_2, by taking $g_2 = 0$, is shown with the gray shade overlapped on the total systematic error. The model curve is also shown as a line through data points. The top plot shows values also multiplied by 15.134 for unit conversion to [10^{-4} fm^4]. The bottom plot is just the integral part, without the kinematic factor taken into account.

resonance region and how, on average, it connects with the DIS limit. They can constrain NLO fits (including higher twist corrections) of spin structure functions to extract polarized PDFs, and they shed new light on the valence quark structure of the nucleon at large x.They can be used to study quark-hadron duality and to extract matrix elements in the framework of OPE.

We use our data on the deuteron, together with a detailed fit of the corresponding proton data, to extract neutron spin structure functions, using a convolution model. These results access, for the first time, inclusive neutron spin structure in the resonance region. They can also be used to cross check the results from ^{3}He targets at high x.

Our data allow very precise determination of moments of g_{1d} and g_{1n}, which can be used to test the approach to the GDH sum rule limit, χPT and phenomenological models and to extract matrix elements in the framework of OPE. We find that χPT describes our results for Γ_1 only up to very moderate $Q^2 \approx$?? and is unable to explain the values obtained for the polarizability γ_0 at and near the photon point.

Further data will come from the analysis of the EG4 experiment with CLAS, which will extend the kinematic coverage of the present data set to even lower Q^2 for a more rigorous test of χPT. At the highest values of Q^2, data from the recently completed experiment EG1-DVCS will improve our knowledge of A_1 at large x and further reduce the uncertainty with which g_{1p} is known in the DIS region. Finally, additional information on the structure functions g_2 and A_2 is forthcoming once experiment "SANE" in Hall C and experiment "g2p" in Hall A (which begins running this Fall) have been analyzed. A complete mapping of spin structure functions in the valence quark region, out to the highest possible x, is one of the corner stones of the program with the energy-upgraded 12 GeV accelerator at Jefferson Lab.

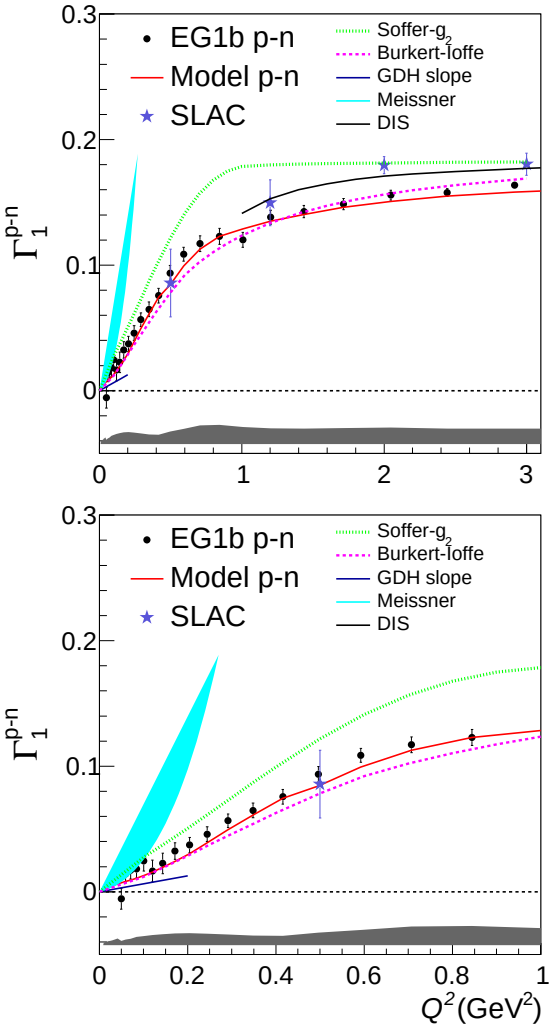

FIG. 22: Γ_1^{p-n} for the versus Q^2 from data and data+model.

Acknowledgments

We would like to acknowledge the outstanding efforts of the staff of the Accelerator and the Physics Divisions at Jefferson Lab that made this experiment possible. This work was supported in part by the U.S. Department of Energy and the National Science Foundation, the Italian Instituto Nazionale di Fisica Nucleare, the French Centre National de la Recherche Scientifique, the French Commissariat à l'Energie Atomique, the Emmy Noether grant from the Deutsche Forschungs Gemeinschaft and the Korean Science and Engineering Foundation. The Southeastern Universities Research Association (SURA) operates the Thomas Jefferson National Accelerator Facility for the United States Department of Energy under contract DE-AC05-84ER-40150.